

Classical patterns in the quantum rainbow channeling of high energy electronsM. Ćosić¹ and S. Petrović¹*Department of Physics, “VINČA” Institute of Nuclear Sciences National Institute of the Republic of Serbia, University of Belgrade, Belgrade, Republic of Serbia*Y. Takabayashi²*SAGA Light Source, 8-7 Yayoigaoka, Tosu, Saga 841-0005, Japan*

(Received 9 September 2020; accepted 26 January 2021; published 15 February 2021)

We are investigating the quantum dynamics of a well-collimated electron beam transmitting through planar channels of the Si crystal. Electron states were represented by wave packets while the electron beam is treated as an ensemble of noninteracting wave packets. We have investigated the relationship between classical caustic pattern and anharmonicity of the potential and analyzed how quantum dynamic depends on the wave packet impact parameter and beam’s angular divergence. We found that the extrema of the electron trajectory period, considered as a function of the impact parameter, determine the shape of the caustic pattern. All wave packet probability densities have multiple maxima generated by a self-interference. Their sum, that represents probability density of an ensemble, was found to depend strongly on the beam angular divergence. For small divergence, most peaks of different wave packets are aligned causing wavelike behavior of the ensemble. For moderate angular divergence maxima of some wave packets, are aligned with minima of others, resulting in the emergence of the classical caustic pattern. We have shown and experimentally confirmed that the only indication that the observed caustic pattern is generated by the quantum dynamics is a slight systematic shift of the corresponding caustic maxima.

DOI: [10.1103/PhysRevA.103.022818](https://doi.org/10.1103/PhysRevA.103.022818)**I. INTRODUCTION**

It is generally believed that low energy scattering is governed by the nonrelativistic quantum mechanics. For larger energies, the full quantum treatment is no longer necessary, since the semiclassical approximation becomes sufficiently accurate. In the semiclassical framework, a quantum wave function is constructed from the corresponding family of classical phase space trajectories [1]. It describes small corrections to the classical dynamics arising due to the particle’s wave nature. For even larger energies the wave corrections become negligible and particle scattering can be adequately described in the terms of classical mechanics.

In this publication, we will focus on the transition between classical and quantum mechanics. The quantum-classical correspondence is usually studied in the framework of the semiclassical approximation with a plane wave representing the classical ensemble. However, the semiclassical-classical transition is singular [2,3]. It is mathematically equivalent to a limit $\hbar \rightarrow 0$, with a physically meaningless limiting value $\hbar = 0$ since it removes terms describing spatial and temporal variations of the wave function. This singularity obstructs a complete understanding of the emergence of the classical level of reality. This is the reason why a great majority of studies were investigating which new phenomena emerge on the route to the classical limit [4].

Note that the standard paradigm describes how single-particle behavior changes in different energy ranges. Here, we would like to point out a different possibility for the emergence of classical behavior. According to J. von Neumann, the causality of the macroscopic world is just an illusion created by a leveling action of the law of large numbers which obscures the true nature of elementary processes operating simultaneously [5]. Therefore classical behavior emerges naturally in the ensemble of quantum particles. Under certain conditions interaction between ensemble members behaves as a continuous monitoring apparatus inducing continuous quantum-classical transition. This approach is elaborated in the so-called decoherence theory [6].

Note that there exists a third possibility. The classical structures can emerge on the level of ensemble out of purely quantum dynamics of noninteracting wave packets and are a consequence of its structural stability [7]. Structurally stable systems have a special property that their topological features are unaffected by relatively large variations of system parameters. However, even for infinitesimal changes of critical values of parameters, the morphology of the system changes dramatically [8–10].

A system suitable for this kind of investigation is particle transmission of channeled particles through thin nanostructured materials in the regime of low current where particles can be considered as independent. Channeled particles perform bounded motion in potential wells of atomic planes [11] and have well-defined trajectories. In the classical description of these systems, structural stability manifests itself in the

*Corresponding author: mcosic@vinca.rs

form of caustic lines [12]. In the quantum domain, classical caustics are just a skeleton onto which quantum interference is superimposed [13]. Existence of the rainbow lines underlays all manifestations of optical [14], atomic [15], nuclear [16], surface [17], and crystal rainbow effects [18–20]. Crystal rainbow effect has been experimentally confirmed many times [21–25], and channeling experiments are now relatively straightforward to perform.

In the past, the rainbow scattering of high energy electrons in crystals has been investigated by the Kharkov group [26–28]. In their approach, an electron beam was represented by a plane wave, and interpretation of the effect was based on the detailed comparative study of classical and quantum results. It should be mentioned that the Belgrade group has pioneered a different approach. They have represented a beam of positively charged particles by an ensemble of noninteracting wave packets and analyzed the obtained family of quantum wave functions using tools borrowed from singularity theory and topology. It has been found that coordination of wave packets self-interference is the key concept allowing the explanation of the quantum crystal rainbow effect [29,30] which will be used also for the analysis of the quantum-classical transition.

We have investigated the transmission of 255-MeV electron beam in a direction parallel to the (110) plane of thin Si crystal. Electrons were represented by wave packets, while the electron beam was treated as an ensemble of noninteracting wave packets. This choice corresponds to a setup of a recent experiment in which the crystal rainbow effect with electrons was observed for the first time and interpreted in the framework of the classical mechanics [31].

We will show that another interpretation of the experimental results is possible. Namely, that classically behaved patterns can be produced on the level of the ensemble by the coordinated self-interference of wave packets. The obtained interpretation was also experimentally tested. In the experiment, well collimated 255-MeV electron beam was transmitted through planar channels {220} of the 470-nm-long Si crystal, and the angular distribution of transmitted electrons was recorded. We will show that result of quantum simulation fit much better experimental data than the corresponding result of the classical simulation. It will be also shown that the angular divergence of the incoming beam influences the level of coordination between wave packet self-interference. For the maximal level of coordination the wave nature of electrons is amplified in the ensemble producing a wavelike distribution of transmitted electrons.

II. THEORETICAL FRAMEWORK

Let a_L , and N_a denote lattice constant and a number of atoms in the unit cell of the Si crystal. Viewed in the direction parallel to the plane (110), the arrangement of atoms form a set of planes {220}. Spacing between them is $d_{220} = \sqrt{2}a_L/4$, while corresponding surface density is $\sigma_{220} = N_a d_{220}/a_L^3$.

We assume that the $y0z$ plane of the Cartesian coordinate system is attached to the (220) plane of the Si crystal. A quasiparallel electron beam of kinetic energy $E_k = 255$ MeV was assumed to be aligned with the z axis of the coordinate

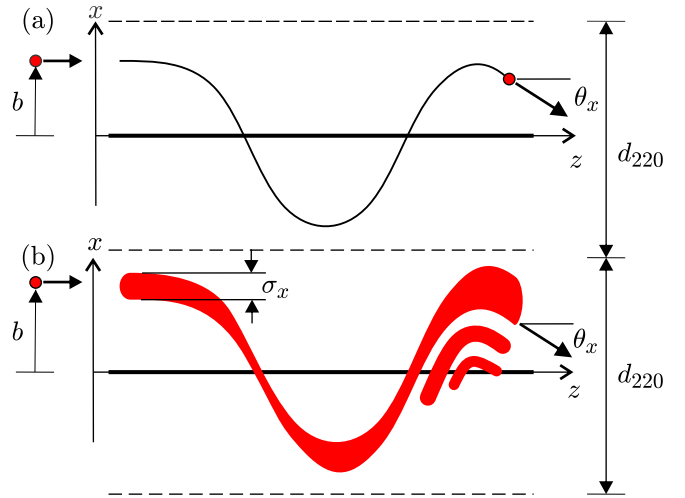


FIG. 1. (a) Schematic representation of the classical channeling process. The thin black line shows the trajectory of initial position b and exiting angle θ_x . (b) Schematic of the quantum channeling process. Red (gray) lines show probability density that has an initial mean value of position b , spatial standard deviation σ_x , and have a mean value of the exiting angle θ_x . Thinner red (gray) lines show self-interference peaks. The thick black lines show positions of atomic planes {220}. The dashed lines show the boundaries of the planar channel.

system. Consequently, the x axis of the coordinate system is orthogonal to the crystal planes. In the laboratory system the relativistic electron mass m_r and longitudinal linear momentum p_z are given by expressions

$$m_r = m_e \left(1 + \frac{E_k}{m_e c^2} \right), \quad p_z^2 = 2m_e E_k \left(1 + \frac{E_k}{2m_e c^2} \right), \quad (1)$$

where m_e is electron rest mass and c is vacuum light velocity.

The electron-crystal interaction potential was constructed from Molière's approximation of Thomas-Fermi's electron-Si interaction potential [11,32]

$$U(\mathbf{r}) = -\frac{Z_2 e^2}{4\pi \epsilon_0 |\mathbf{r}|} \sum_{n=1}^3 \alpha_n \exp\left(-\beta_n \frac{|\mathbf{r}|}{a_s}\right), \quad (2)$$

where $\mathbf{r} = (x, y, z)$ denotes the electron-Si separation vector, $Z_2 = 14$ is Si atomic number, e is elementary charge, ϵ_0 is vacuum permittivity, $\alpha = (0.35, 0.55, 0.1)$ and $\beta = (0.3, 1.2, 6)$ are dimensionless Molière's fitting parameters, $a_s = \frac{\epsilon_0 \hbar^2}{m_e e^2} \sqrt[3]{\frac{9\pi^5}{2Z_2}}$ is screening length, and \hbar is reduced Planck's constant.

Channeled particle undergoes through a series of correlated small angle scattering on atoms forming atomic strings or planes which keeps particle's transverse energy conserved [11]. As a result, channeled particles perform bounded motion in the potential well of the crystal plane. The schematic of the classical channeling effect is shown in Fig. 1(a). Since scattering angles are small, the continuous approximation could be applied [33]. The resulting thermally averaged potential of a

single crystal plane is given by the expression [34]

$$V_{220}^{\text{th}}(x) = -\frac{Z_2 e^2 a_s}{4\sqrt{2}\epsilon_0 d_{111}^2} \sum_{n=1}^3 \frac{\alpha_n}{\beta_n} \exp\left[\frac{\beta_n^2 \sigma_{\text{th}}^2}{2a_s^2}\right] \times \left\{ \exp\left[-\frac{\beta_n |x|}{a_s}\right] \operatorname{erfc}\left(\frac{\beta_n \sigma_{\text{th}}}{\sqrt{2}a_s} - \frac{|x|}{\sqrt{2}\sigma_{\text{th}}}\right) + \exp\left[\frac{\beta_n |x|}{a_s}\right] \operatorname{erfc}\left(\frac{\beta_n \sigma_{\text{th}}}{\sqrt{2}a_s} + \frac{|x|}{\sqrt{2}\sigma_{\text{th}}}\right) \right\}, \quad (3)$$

where erfc stands for complementary error function [35], and σ_{th} is the standard deviation of the Si atoms thermal vibration given by the expression

$$\sigma_{\text{th}}^2 = \frac{3\hbar^2}{A_r m_u k_B \Theta_D} \left(\frac{\Theta_D}{T} D_f(T/\Theta_D) + \frac{1}{4} \right), \quad (4)$$

here $A_r = 28.0855$ is atomic weight of Si atom, $m_u = 1.6605 \times 10^{-27}$ kg is universal atomic mass unit, $\Theta_D = 543$ K is Si the Debye temperature [11], $k_B = 1.3806 \times 10^{-23}$ J/K is Boltzmann's constant, T is crystal's absolute temperature, and D_f is the Debye's function. The potential of the planar channel was expressed as a sum of potentials of individual atomic planes. In the laboratory coordinate system, the potential of the channel is given by the following expression

$$V(x) = \sum_{m=-N}^N V_{220}^{\text{th}}(x - m d_{220}) - \bar{V}. \quad (5)$$

Constant $\bar{V} = \sum_m V_{220}^{\text{th}}(m d_{220})$ was introduced in order to have $V(0) = 0$, and $2N + 1$ is a number of neighboring planes contributing significantly to the scattering process.

The maximal deflection angle a channeled particle could have is small. It is given by the expression

$$\Theta_c = \sqrt{\frac{V_0}{E_k}}, \quad (6)$$

where $V_0 = V(d_{220}/2)$, and it is called the critical channeling angle. Instead of the time, t , classical and quantum dynamics will be parameterized by variable $\tau = \frac{1}{2\pi} \omega t$ called the reduced time [36], where

$$\omega = \sqrt{\frac{\partial_x^2 V(x)}{m_r}} \Big|_{x=0}, \quad (7)$$

is an angular frequency of electron trajectories in the center of the potential well.

Here, we are investigating the dynamics of the electron beam for $0 \leq \tau \leq 2$. During this time most of the electron trajectories will perform less than two full oscillations in the transverse plane. For a such short times electronic, nuclear, and radiative energy losses, together with the fluctuations of the electron scattering angle can be neglected, and longitudinal linear momentum is approximately conserved.

In the transverse direction, classical dynamics is governed by Hamilton's equations

$$\frac{d}{d\tau} \theta_x = -2\pi \frac{\partial_x V(x)}{\sqrt{2m_r \omega^2 E_k}}, \quad \frac{d}{d\tau} x = 2\pi \sqrt{\frac{2E_k}{m_r \omega^2}} \theta_x, \quad (8)$$

where $\theta_x = p_x/p_z$ is current scattering angle. When beam is parallel solutions of the Eqs. (8) give family of trajectories parameterized only by the impact parameter b . For any fixed value of the variable τ , the trajectory family defines two maps. A map of the electron initial position b to its current position $X(b) \equiv x(\tau; b)$ and current scattering angle $\Theta_x(b) \equiv \theta_x(\tau; b)$ that are called spatial and angular deflection functions, respectively. Points of their respective equilibrium sets, defined by equations $\partial_b X(b) = 0$, $\partial_b \Theta_x(b) = 0$, are called spatial and angular rainbows. Their trajectories define lines called caustics [37]. On the line, the density of electron trajectories is infinite. Therefore the probability of finding a classical particle on the caustic line is very large.

In the quantum description, electrons are represented by the wave packets parameterized also by the impact parameter b . Schematic of the process is given in Fig. 1(b). In the spatial representation, the dynamics of the electron transverse quantum state ψ_b is governed by the Schrödinger equation

$$i\partial_\tau \psi_b(x, \tau) \frac{\hbar\omega}{2\pi} = \left[-\frac{\hbar^2}{2m_r} \partial_x^2 + V(x) \right] \psi_b(x, \tau). \quad (9)$$

while motion in the longitudinal direction is free. The corresponding wave function in the angular representation $\varphi_b(\theta_x, \tau)$ is given by the integral

$$\varphi_b(\theta_x, \tau) = \sqrt{\frac{k_z}{2\pi}} \int \psi_b(x, \tau) \exp[-ik_z \theta_x x] dx, \quad (10)$$

where $k_z = p_z/\hbar$ is electron's longitudinal wave vector. The initial electron state is given by a Gaussian function

$$\psi_0(x; b) \equiv \psi_b(x, 0) = \frac{1}{\sqrt{\sqrt{2\pi}\sigma_x^2}} \exp\left[-\frac{(x-b)^2}{4\sigma_x^2}\right], \quad (11)$$

of mean value b , and standard deviation σ_x , whose angular representation is

$$\varphi_0(x; b) \equiv \varphi_b(\theta_x, 0) = \frac{1}{\sqrt{\sqrt{2\pi}\sigma_\theta^2}} \exp\left[-\frac{\theta_x^2}{4\sigma_\theta^2} - ik_z \theta_x b\right], \quad (12)$$

where $\sigma_\theta = 1/(2k_z \sigma_x)$.

The reduced angular Hamilton's principal function S_θ is defined by the equation

$$\frac{d}{d\theta_x} S_\theta(\theta_x) = -x(\theta_x). \quad (13)$$

In the initial value, representation [38,39], a semiclassical wave function is given by the integral

$$\psi_b(x, \tau) = \sqrt{\frac{k_z}{2\pi}} \int |\psi_0(\ell; b)| \exp[-ik_z(S_\theta(\ell) - x\Theta_x(\ell))] \times \sqrt{\frac{d\Theta_x(\ell)}{d\ell}} d\ell, \quad (14)$$

where $dS_\theta(b) = X(b)d\Theta_x(b)$. In order that integrand can be considered as rapidly oscillating function, and semiclassical representation (14) valid, it is necessary that size parameter $\varsigma = k_z d_{220} \gg 1$.

The electron beam is represented by an ensemble of noninteracting wave packets. Spatial and angular probability

densities of the ensemble labeled ρ_x and ρ_θ , respectively, are given by relations

$$\begin{aligned}\rho_x(x, \tau) &= \sum_b p_b |\psi_b(x, \tau)|^2, \\ \rho_\theta(\theta_x, \tau) &= \sum_b p_b |\varphi_b(\theta_x, \tau)|^2,\end{aligned}\quad (15)$$

where p_b are statistical weights of states ($\sum_b p_b = 1$). We have assumed that the incoming electron beam has a Gaussian profile of small angular divergence Ω . It is easy to show that initial angular distribution $\rho_\theta(\theta_x, 0)$ is given by the expression

$$\rho_\theta(\theta_x, 0) = \frac{1}{\sqrt{2\pi}\sigma_\theta} \exp\left[-\frac{\theta_x^2}{2\sigma_\theta^2}\right], \quad (16)$$

giving $\sigma_\theta = \Omega$, and $\sigma_x = 1/(2k_z\Omega)$. At the entrance plane of the crystal, the spatial distribution of the electron beam is practically uniform. If impact parameters form regular grid of M points and statistical weights are all equal to $p_b = 1/M$ then for sufficiently large M the difference between $\rho_x(x, 0)$ and the uniform distribution is negligible in the interval $-d_{220}/2 \leq x \leq d_{220}/2$ [13].

III. RESULTS

The lattice constant of the Si crystal is $a_L = 0.5431$ nm, and the number of atoms per unit cell is $N_a = 8$. Corresponding interplanar distance and planar surface density are $d_{220} = 0.1920$ nm, and $\sigma_{220} = 9.5893$ nm⁻², respectively. The screening length is $a_s = 19.4388$ pm, while amplitude of the thermal vibrations at the room temperature ($T = 301$ K) is $\sigma_{th} = 7.5815$ pm. It was found that $N = 3$ is sufficient for convergence of the interaction potential (5).

For 255-MeV electrons, the relativistic mass is $m_r = 500.0226 m_e$, and relativistic factor is $\beta_z = v_z/c = 0.999998$, where v_z is longitudinal electron velocity. The corresponding critical channeling angle is $\Theta_c = 0.2981$ mrad, while $\tau = 2$ corresponds to the crystal thickness of $L = 708.3773$ nm.

The ionization energy loss of channeled electrons can be estimated using the relativistic form of the Bethe-Bloch formula

$$S_i = -\frac{dE}{dz} = \frac{4\pi Z_2 N_a}{m_e c^2 \beta_z^2 a_L^3} \left(\frac{e^2}{4\pi\epsilon_0}\right)^2 \left[\ln\left(\frac{2m_e c^2 \beta_z^2}{(1-\beta_z^2)I}\right) - \beta_z^2 \right], \quad (17)$$

where S_i is ionization stopping power, $I = 172.25$ eV is the average ionization energy of the Si atom [40]. Traversing the crystal electrons will lose approximately

$$\Delta E_i = \int_0^L S_i dz = 508.6857 \text{ eV}. \quad (18)$$

To estimate radiation energy losses we shall employ the harmonic approximation [41], and represent potential (5) in the interval $-d_{220}/2 \leq x \leq d_{220}/2$ by the expression $V(x) \approx 4V_0 (x/d_{220})^2$. The relative difference between actual and approximative potential is very small everywhere except near points $\pm d_{220}/2$. At any instance of time, the radiated power is given by the relativistic Larmor formula [42]. For parallel beam, the transverse part of the electron trajectory is given

by the expression $x_b(\tau) = b \cos(2\pi\tau)$, and electron accelerate only in transverse direction. In that case, the radiated power P_b is given by the relation

$$P_b = -\frac{dE}{dt} = \frac{e^2 \omega^4}{96\pi^5 \epsilon_0 c^3} \left[\frac{d^2 x_b(\tau)}{d\tau^2} \right]^2. \quad (19)$$

The total radiated energy by the electron beam is given by the relation

$$\begin{aligned}\Delta E_r &= \frac{2\pi}{d_{220}\omega} \int_0^2 \int_{-d_{220}/2}^{d_{220}/2} P_b(\tau) db d\tau \\ &= \frac{e^2}{9\epsilon_0 d_{220}} \frac{(8V_0/m_e c^2)^{3/2}}{(1-\beta_z^2)^{5/4}} = 97.7765 \text{ eV}.\end{aligned}\quad (20)$$

Therefore, total energy loss of the electron beam $\Delta E = \Delta E_i + \Delta E_r = 606.4622$ eV is utterly negligible in comparison to $E_k = 255$ MeV, and can be safely neglected.

Note that harmonic approximation is inadequate for the analysis of the rainbow effect, since it allows only point caustic, i.e., point singularities [30]. According to Whitney's theorem, the slightest perturbation transform point into the structurally stable line singularities [43,44].

A. The classical solution

In the classical approach, Hamilton's equations (8) were solved numerically by the Runge-Kutta method of the fourth order [45]. Figures 2(a) and 2(b) show obtained spatial and angular trajectory families whose impact parameters uniformly cover the interval $-d_{220}/2 \leq x \leq d_{220}/2$. Dotted lines show caustics generated by the respective trajectory families. The caustic pattern consists of a repeated appearance of pairs of caustic lines. In Fig. 2(a), there are four pairs of caustic lines labeled $(\mu_1, \mu'_1), \dots, (\mu_4, \mu'_4)$, respectively. Lines of each pair are joined at points M_1, \dots, M_4 forming the shape equivalent to the bifurcation set of the cusp catastrophe [9]. Spatial distribution is large on caustic lines, and electron beam is focused to the maximal extent at points M_1, \dots, M_4 . Caustic pattern in Fig. 2(b) consists of line pairs $(\nu_1, \nu'_1), \dots, (\nu_3, \nu'_3)$ joined at points N_1, \dots, N_3 . Note that only the cusp point N_4 of the fourth caustic pair is visible in Fig. 2(b). The line pair (ν_0, ν'_0) is slightly different in origin. It exists because the initial electron beam is parallel. Besides the coordinate origin, the beam's angular divergence is very small at points N_1, \dots, N_4 . Although the evolution of the electron beam is aperiodic, new cusped caustic lines appear with perfect periodicity. The time interval required for the birth of a new caustic pair is equal to 0.5. Therefore the evolution of the caustic lines progresses cyclically with each repetition called the rainbow cycle [46].

Figures 2(c) and 2(d) show the spatial and angular deflection functions for $\tau = 2$. In both cases, the obtained functions have eight extrema. They are labeled μ_1, \dots, μ_4 and ν_0, \dots, ν_3 , respectively while symmetrical extrema are additionally marked by prime. Note that the ordinate of each rainbow point is equal to the ordinate of the corresponding point on the caustic line.

In Refs. [12], morphological properties of the trajectory family were investigated in detail. For positively charged

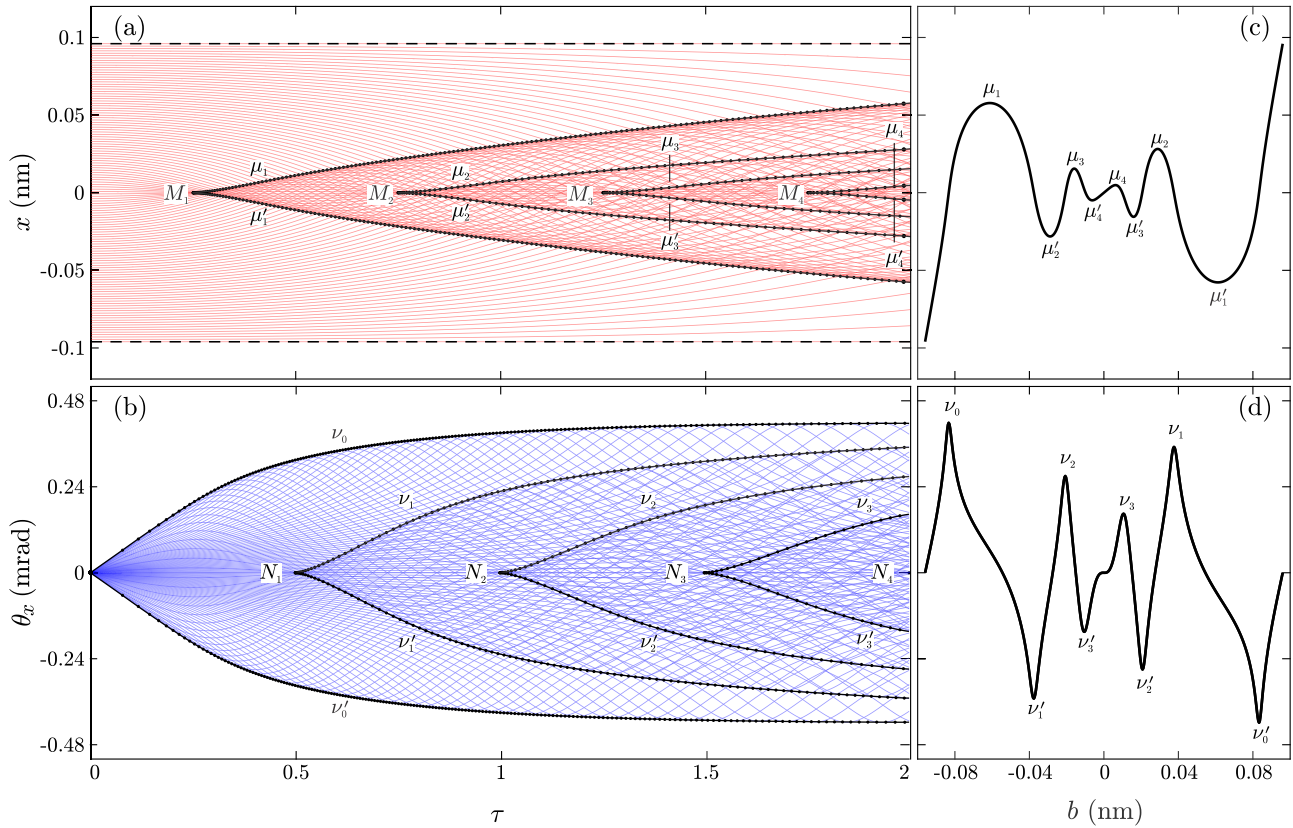


FIG. 2. Family of the classical electron trajectories in (a) spatial and (b) angular space for $0 \leq \tau \leq 2$. The dotted black lines show caustic lines of respective families. (c) The spatial and (d) angular deflection function. The thin dashed black lines show locations of (220) planes.

particles, the interaction potential is given by equation $V_p(x) = -V(x - d_{220}/2)$. Although potentials $V(x)$ and $V_p(x)$ are very similar, their caustic patterns are very different. For potential $V_p(x)$ caustic pattern consist of a repeated appearance of the bifurcation set of the A_5 catastrophe, called the butterfly [9] (see Fig. 2 of Ref. [12]). Caustic pattern shown in Fig. 2 is equivalent to caustics generated by the harmonic potential $V_h(x) = V_0 \cos(k_x x)$ [36,47].

The observed difference between caustic patterns can be explained by the fact that the dependence of the period of electron trajectory T on the impact parameter b , defined by the integral

$$T(b) = \sqrt{8m_r} \int_0^b \frac{dx}{\sqrt{V(b) - V(x)}}, \quad (21)$$

has only one critical point, while in the case of the potential $V_p(x)$ the corresponding dependence $T_p(b)$ have three. In Appendix A, it has been shown that number of cusps of the caustic pattern is equal to the number of extrema of the function $T(b)$.

Note that rainbow condition $\partial_b x(\tau; b) = 0$ defines a limiting curve formed by intersection points of neighboring trajectories [48]. It is a property of the ensemble of trajectories not reducible to the property of any individual ensemble member. Therefore it is no surprise that information about the shape of the caustic pattern is contained in the function $T(b)$ which describes the behavior of the ensemble.

Any perturbation of the potential, regardless of its size, produces the caustic pattern topologically equivalent to the unperturbed case. To change the shape of the caustic pattern it is necessary that perturbation forces bifurcation of extrema of the function $T(b)$. Since this process is discrete, the change of the caustic shape can happen only abruptly, i.e., it is structurally stable. This is a deep topological reason why analysis of the caustic pattern for the parallel beam is useful for analysis of the more complicated case when energy loss and beam divergence are not neglected [12,23,31]. Here, we will demonstrate its usefulness for the explanation of how classical structures emerge out of the quantum dynamics of ensemble members.

B. The quantum solution

First, we will analyze the transmission of an electron beam having angular divergence $\Omega = 0.25\Theta_c$, which is approximately equal to the beam divergence reported in Ref. [31]. The longitudinal wave vector is $k_z = 1.2948 \text{ fm}^{-1}$, giving the initial spatial standard deviation $\sigma_x = 5.1816 \text{ pm}$ and the size parameter $\zeta = k_z d_{220} \approx 250\,000$.

In the case of positrons, the largest contribution to the quantum rainbow peak in the ensemble distribution comes from the wave packet having an impact parameter of the classical rainbow [13,29]. Thus, we have followed the evolution of the wave packet of impact parameter corresponding to an abscissa of the rainbow point μ'_1 from Fig. 2(c) equal to $b_0 = d_{220}/3$. The time-dependent Schrödinger equation (9)

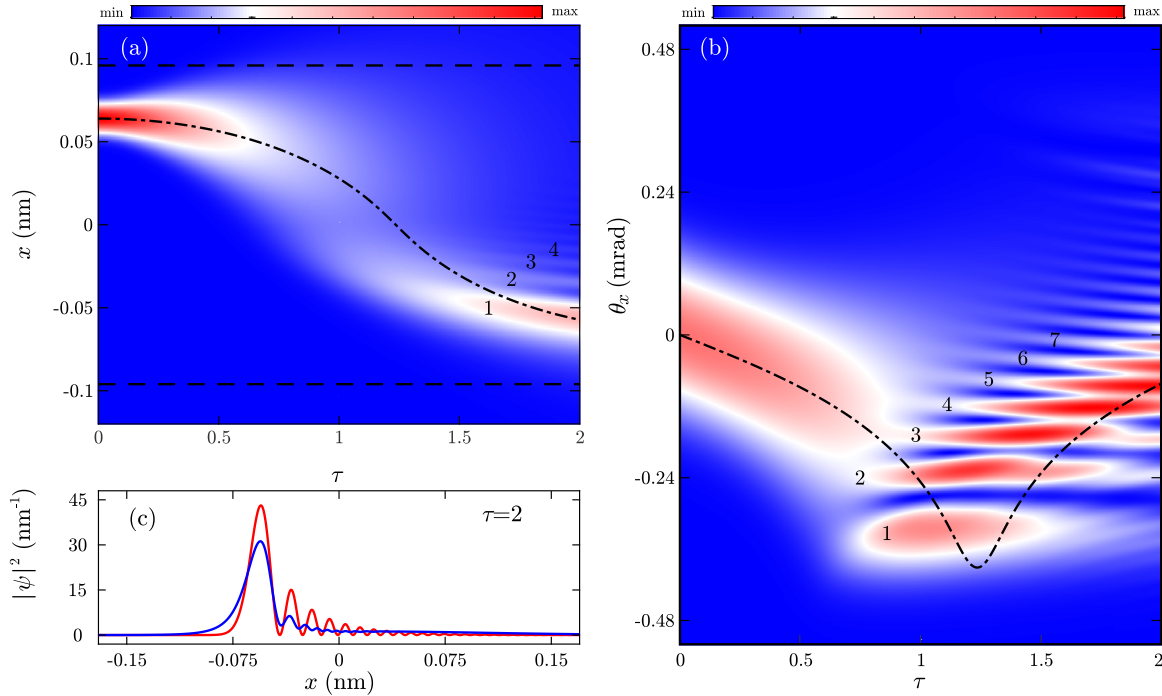


FIG. 3. Evolution of the wave packet $b = d_{220}/3$ in the (a) spatial and (b) angular representations. The thin dashed black lines show locations of (220) planes. The thin dot-dashed black lines show the corresponding trajectory of the classical particle. (c) The blue (dark gray) line: section through exact probability density from Fig. 3(a) for $\tau = 2$. The red (gray) line: the corresponding semiclassical result.

was solved numerically by the method of Chebyshev global propagation [49,50], and obtained evolution is shown in Fig. 3.

Self-interference effects are not visible for $\tau \leq 1$, while for $\tau > 1$ they are very pronounced. At the same time, the dominant maximum of the wave packet roughly follows the trajectory of the corresponding classical electron. Since the system is conservative and quantum mechanical tunneling

is negligible, the maximal negative deflection of the wave packet is equal to its maximal positive deflection.

Since the size parameter ζ is large, an excellent approximation of the numerically obtained solution is given by the semiclassical approximation. In Appendix B, it has been shown that for $\tau = 2$ semiclassical probability density of the wave packet from Fig. 3(a) is given by the following expression

$$|\psi_{b_0}(x)|^2 \approx \sqrt{\frac{\pi|p_1|^2}{2\Omega^2|\gamma_1|^4}} \exp\left[-\frac{p_1}{4\gamma_1^3\Omega}\left(x - q_0 - \frac{2}{3}\gamma_2\right)\right] \text{Ai}^2\left[-\frac{p_1}{2\gamma_1\Omega}(x - q_0 - \gamma_2)\right], \quad (22)$$

here $\gamma_1 = -\sqrt{|r_3|/8\Omega^3k_z^2}$ is dimensionless parameter while parameter $\gamma_2 = \Omega/8\gamma_1^3p_1$ have the same physical dimension as the spatial coordinate. Parameter $r_3 = 2p_1q_2/2$, p_1 is the first derivative of the angular deflection function $\Theta_x(b)$ at the point b_0 , while $q_0 = X(b_0)$, and q_2 is second derivative of the spatial deflection function $X(b)$ at the point b_0 . Note that p_1 is negative while q_2 is positive [see Fig. 2(b)] and γ_2 is small comparable to q_0 . As a consequence, for $x > q_0$ oscillations of the Airy function are damped by the exponential factor, while for $x < q_0$ a growth of the exponential factor is overcompensated by super-exponential decay of the Airy function. Figure 3(c) shows that the obtained approximate solution corresponds perfectly to the behavior of the numerically obtained solution.

One heuristic interpretation of the size parameter claims that ζ gives a number of excited transverse states needed to be

taken into account when calculating scattering amplitudes [1]. On the grounds of the correspondence principle [3,51], one can be tempted to assume that both exact and semiclassical solution should resemble very closely the classical solution. However, this is not necessarily true. Energy eigenvalues and eigenvectors are solutions of the equation

$$\left[-\frac{\hbar^2}{2m_r}\partial_x^2 + V(x)\right]\psi_n(x) = E_n\psi_n(x). \quad (23)$$

Any quantum state can be represented as a superposition $\psi(x) = \sum_n c_n \psi_n(x)$, where $\sum_n |c_n|^2 = 1$. Explicit expansion of the state ψ_{b_0} in the numerically obtained states ψ_n shows that truncated basis $0 \leq n \leq 1001$ is almost complete. The norm of the state in the orthogonal complement is $\sum_{n=1002}^{\infty} |c_n|^2 \leq 3 \times 10^{-10}$. However, out of 1001 states considered explicitly, 26 of them have $|c_n|^2 \geq 10^{-6}$,

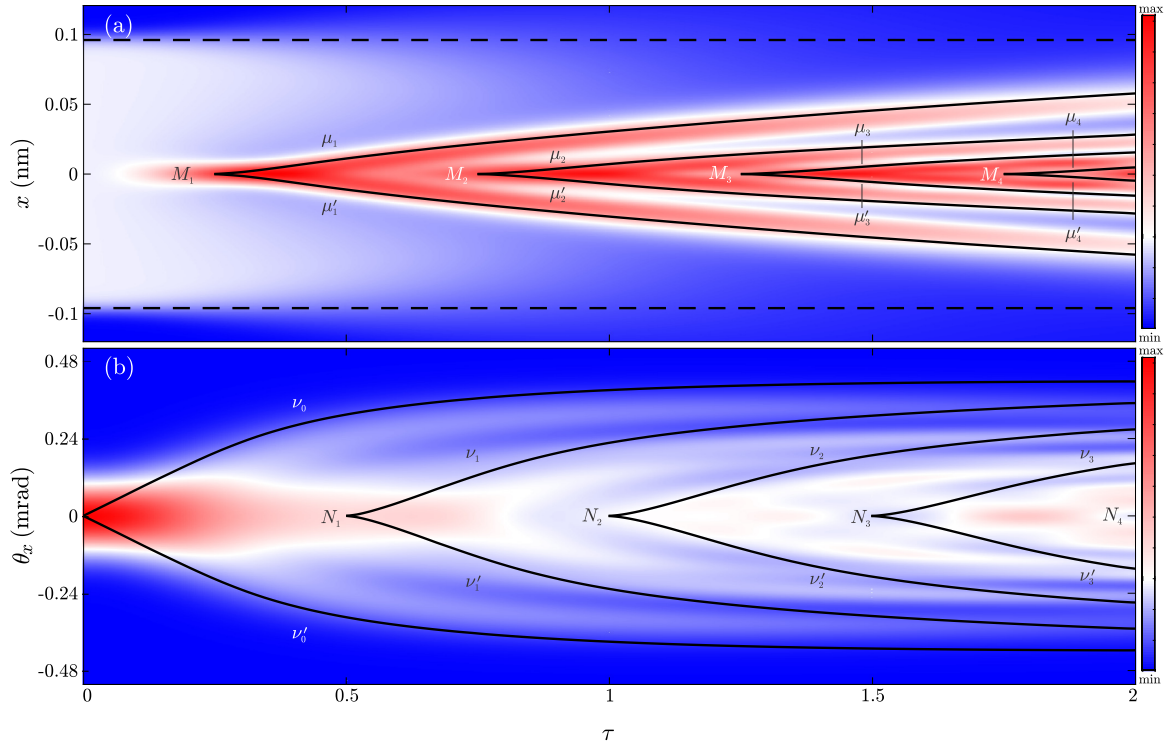


FIG. 4. An evolution of a probability density of the electron beam for $\Omega = 0.25\Theta_c$ transmitting through planar channels $\{220\}$ of the Si crystal in the (a) spatial and (b) angular representations, respectively. Dashed black lines show locations of $\{220\}$ planes. Thick black lines show classical caustic lines from Fig. 2.

($n \in \{1, \dots, 30, 33\}$), while only states $n \in \{12, \dots, 15\}$ have $|c_n|^2 \geq 0.1$. Therefore, the number of excited states is far smaller than $\zeta = 250\,000$, and the correspondence principle can not be invoked.

If examined carefully the classical results can be obtained only in the limiting process $k_z \rightarrow \infty$. In the Appendix C it was shown that semiclassical wave function (22) has the correct classical limit. The space between zeros of the Airy function shrinks by the factor $k_z^{2/3}$ while the amplitude of the largest maximum grows asymptotically as $k_z^{1/4}$. For $x \neq q_0$ values of the Airy function are damped asymptotically by the exponential factor whose exponent is proportional to k_z . In the limit $k_z \rightarrow \infty$ for $x \neq q_0$, $|\psi_{b_0}|^2 \rightarrow 0$ while for $x = q_0$, $|\psi_{b_0}|^2 = O(k_z^{1/2}) \rightarrow \infty$. Therefore the considered value of the k_z is by far too small that $|\psi_{b_0}|^2$ from Fig. 3 that can be approximated by the dot-dashed line from the same figure.

Another heuristic interpretation of the size parameter is that $\theta_0 = \zeta^{-1}$ is roughly proportional to the angular size of the smallest feature of the far-field diffraction pattern [52,53]. For example, the size of the diffraction peak, generated by scattering on an obstacle of width d , is equal to $\pi\zeta^{-1}$.

If maxima of the angular probability density, visible for $\tau > 1$, were produced by the constructive interference of diffracted waves, then their positions should be given by the Bragg's law. According to it positions of the diffracted maxima (for $n = 0, \pm 1, \pm 2, \dots$) should be located at $\theta_n = n\pi\zeta^{-1} \approx 0.0126n$ mrad. Figure 3(b) shows that there are no maxima at Bragg's angles θ_n . Note that the resolution of the numerical solution is sufficiently high to reveal if any of such peaks is present.

We shall now show that it is possible to give a simple explanation of the size of typical peaks shown in Fig. 3(b). The crucial parameter to be examined is the transverse energy of electrons defined by the following expression

$$E_t(b, \sigma_x) = \frac{\hbar^2}{8m_r\sigma_x^2} + \int_{-\infty}^{\infty} V(x)|\psi_0(x)|^2 dx. \quad (24)$$

Explicit evaluation for the state ψ_b gives $E_t \approx E_{14}$. Now we make very crude approximation that average size of peaks of the distribution $|\psi(x)|^2$ is equal to average peak size of the distribution $|\psi_{14}(x)|^2$ [36,54]. This eigenstate has 14 nodes so the size of its typical peak is approximately given by $\delta x = d_{220}/15 = 0.0128$ nm. Dominant peaks in the probability distribution shown in Fig. 3(a) are labeled 1, ..., 4. Their average width is $\delta \bar{x} = 0.0129$ nm, which is very close to the estimated value. In the case of probability distribution in the angular representation $|\varphi(\theta_x)|^2$, the dominant part of the state norm comes from the interval $[-\Theta_c, \Theta_c]$. Applying the same logic as in the case of spatial representation the size of the typical peak should be $\delta \theta_x = 2\Theta_c/15 = 0.0397$ mrad. This value is remarkable close to the average size of dominant peaks, labeled 1, ..., 7 in the Fig. 3(b) which is equal to $\delta \theta_x = 0.0409$ mrad.

Figure 4 shows probability density of the electron beam obtained by adding probability densities of 301 wave packets, according to Eq. (15). Dominant peaks of the spatial distribution, shown in Fig. 4(a), follow classical caustic lines almost perfectly. As in the classical case, the electron beam is the most focused at points M_1, \dots, M_4 . Widths at the half maximum of quantum caustic peaks are approximately 19%

narrower than the corresponding width of the initial Gaussian wave packet. Note that any manifestations of the electron wave nature are not visible. In the case of the angular distribution, the situation is slightly different. The shape of the obtained distribution still reflects the shape of the corresponding classical caustic pattern. For $\tau \leq 1$, the correspondence between prominent peaks of the distribution and the classical caustic line is almost perfect. Besides the coordinate origin, the electron beam is the most focused near cusp points of classical caustic lines N_1 and N_2 . For $\tau > 1$, the wave nature of electrons starts to manifest itself. In the vicinity of classical caustic lines ν_2 and ν'_2 , there are now two close quantum peaks in place of one. Caustic lines ν_3 and ν'_3 enclose a faint interference pattern consisting of three overlapping peaks forming a “V” shape ridge that runs parallel to the classical caustic line. The largest of these maxima, located at the τ axis, is significantly shifted from the point N_3 where the corresponding classical distribution has maximum. Interestingly, the evolution of the electron beam produces peaks whose widths are significantly smaller than the initial width of wave packets. Therefore obtained quantum distributions are not simply blurred versions of classical densities, obtained by convolution with the Gaussian kernel of standard deviations σ_x or σ_θ , respectively.

If finite resolution and dynamical range of real detectors are taken into the account, it is reasonable to assume that an experimentalist would not be able to identify all those fine details. Observation of the quantum caustic pattern in the full range would require a large number of measurements which may not be practical. Most probably, an experimentalist would have recorded only a few angular distributions corresponding to different values of the τ variable. Only on some of them, he would notice shifts of observed peaks from positions predicted by the classical mechanics, which are only manifestations of the electron wave nature. Such behavior could be easily attributed to an experimental error and disregarded.

To test if it is possible to observe described behavior experimentally, an experiment was designed at SAGA Light Source. A schematic representation of the experimental setup is shown in Fig. 5(a) [31]. The monocrystalline Si membrane was fabricated from a silicon-on-insulator wafer by an etching procedure. The quality of the obtained sample was inspected by x-ray diffraction. The crystal was installed on a two-axis goniometer in a vacuum chamber and rotated to make its (220) planes horizontal. The crystal thickness in the direction of the beam was 470 nm which corresponds to the reduced time $\tau = 1.33$. The 255-MeV electron beam was transmitted through the round-shaped collimator made of tungsten, placed upstream of the target, which produced a beam of constant intensity at the target with the vertical angular standard deviation $\Omega \approx 0.09$ mrad. Angular distributions were measured using a detector consisting of a scintillating screen and a CCD camera placed at $D = 5.12$ m downstream of the crystal. The acquisition of the data from the CCD chip was triggered by beam injection. The angular resolution of the detector was $\Delta\theta_x = 0.0139$ mrad.

The black line in Fig. 5(b) shows a normalized vertical slice through measured angular distribution. The corresponding classical result is in Fig. 5(b) shown by the red line. It was constructed from 200 000 solutions of Eq. (8) where

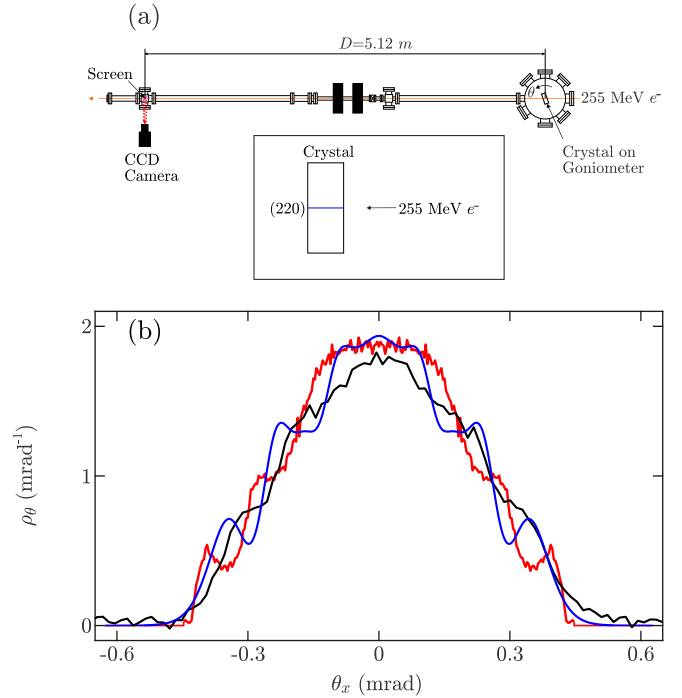


FIG. 5. (a) Schematic of the electron channeling experiment at SAGA Light Source. An angular divergence of the electron beam was $\Omega = 0.09$ mrad $\approx 0.3\Theta_c$. The thickness of the Si crystal was 470 nm, corresponding to $\tau = 1.33$. (b) Normed angular probability densities of the transmitted electron beam: the black line: an experimental result; the red (gray) line: a result of the classical Monte-Carlo simulation; and the blue (dark gray) line: a result of the corresponding quantum simulation.

impact parameters were sampled uniformly from the interval $|b| < d_{220}/2$, while initial angles were sampled from a Gaussian distribution of the standard deviation Ω . The blue line in Fig. 5(b) shows the corresponding result of a quantum simulation constructed from 301 solutions of Eq. (9) according to Eq. (15). Note that the quantum curve fit much better experimental result than the corresponding classical curve, while both of them have essentially the same shape.

IV. DISCUSSION

We have firmly established that the behavior of individual electrons is quantum, i.e. wavelike, while the behavior of the electron beam is classical. To resolve this apparent paradox we need to investigate how self-interference of different wave packets is correlated.

Figure 6 shows the dependence of probability densities on the impact parameter in the spatial and angular representation. For $\tau = 0, 1$, and 2 obtained spatial distributions in the (b, x) space are shown in Figs. 6(a)–6(c), while corresponding angular distributions in the (b, θ_x) space are shown in Figs. 6(d)–6(f). All distributions are invariant on the coordinate transformation $(b, x) \rightarrow (-b, -x)$. These distributions reveal numerous self-interference maxima which confirms the previous finding that the behavior of each electron is wavelike. Maxima of the probability distribution are organized around the classical deflection functions shown by dot-dashed black

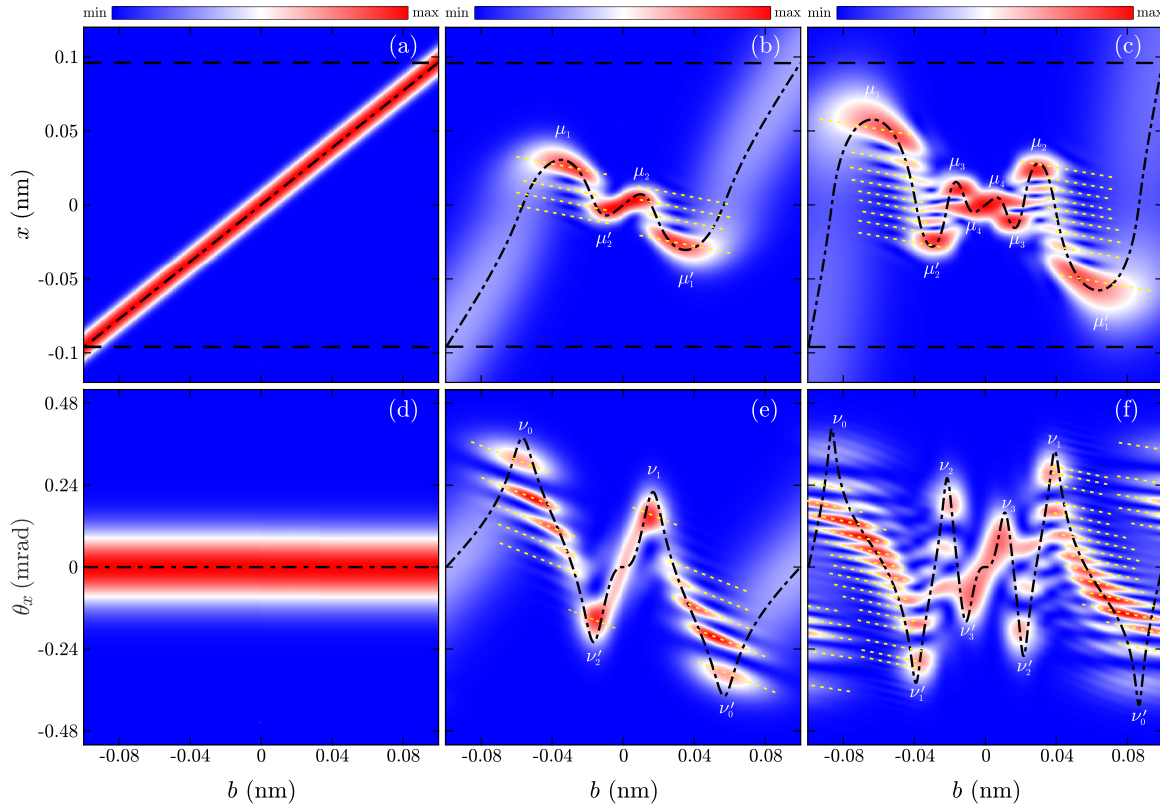


FIG. 6. [(a)–(c)] The quantum spatial deflection maps $|\psi(x, b)|^2$ for $\Omega = 0.25\Theta_c$, at $\tau = 0, 1$, and 2 , respectively. (d)–(f) Corresponding angular quantum deflection maps $|\varphi(\theta_x, b)|^2$. Yellow (light gray) dashed lines show coordination lines. The thick black dot-dashed line shows the classical deflection function. Black dashed lines show locations of (220) planes.

lines. Therefore maps shown in Fig. 6 represent the quantum generalizations of classical deflection functions, and they will be called quantum deflection maps.

Note that wave packets of close impact parameters have almost identical shapes that are slightly shifted. This results in the formation of peaks, elongated in certain directions. The length and direction of the dominant peaks are in Fig. 6 shown by the straight dashed yellow lines, called coordination lines. Their straightness can be explained by the weak dependence of the function $|\psi(x, b)|^2$, and $|\varphi(\theta_x, b)|^2$ on the impact parameter. What is remarkable that in any of Figs. 6(b), 6(c), 6(e), or 6(f) angles between coordination lines and the b axis are equal. Each of Figs. 6(b), 6(c), 6(e), or 6(f) have its own preferable orientation. This angle will be denoted by the letter ϕ and called the coordination angle.

Since statistical weights of all states are equal, relations given by Eq. (15) can be rewritten in the form

$$\begin{aligned} \rho_x(x) &= \frac{1}{d_{220}} \int_{-\frac{d_{220}}{2}}^{\frac{d_{220}}{2}} |\psi(x, b)|^2 db, \\ \rho_\theta(\theta_x) &= \frac{1}{d_{220}} \int_{-\frac{d_{220}}{2}}^{\frac{d_{220}}{2}} |\varphi(\theta_x, b)|^2 db. \end{aligned} \quad (25)$$

These expressions of distributions show more clearly the significance of the coordination lines. Their projections on the vertical axis give information about the location and the width of the peak contributing locally to the total distributions of the transmitted electrons. Their projection on the b axis gives

information on which wave packets are locally strongly coordinated, i.e., it gives information about the height of the resulting local contribution to the distribution of the electron beam. In that regard, there are two possible extreme cases. One corresponds to the coordination angle $\phi = 0$ (or π). In this case, the integral projection of the coordination line produces a peak of the same shape as the considered wave packet peak, while the amplitude of the integral projection is amplified to the maximal possible extent. The opposite extreme case corresponds to the coordination angle $\phi = \pi/2$ (or $-\pi/2$). The local integral projection then distorts the shape of the examined wave packet peak to the maximal extent, producing almost no amplification of its amplitude.

Now we can explain the sequence of quantum deflection functions shown in Fig. 6. The collimation system produces the ensemble of electron wave packets which are coordinated globally. The coordination angles of ensembles in Figs. 6(a) and 6(d) are $\phi = \pi/4$ and $\phi = 0$, respectively. They are equal to the angle between the respective classical deflection function and the b axis. As a result, the integral projection gives a uniform spatial distribution in the region of the channel, thus effectively erasing information about the initial shape of wave packets. On the contrary, the shape of the resulting angular distribution is equal to the initial shape of any of the wave packets. Over time the global coordination gets broken into local domains of strongly coordinated behavior. Figures 6(b), 6(c), 6(e), and 6(f) show that over time the number of coordination lines increases while their length decreases. Note that the coordination angle of lines in Figs. 6(b) and 6(c)

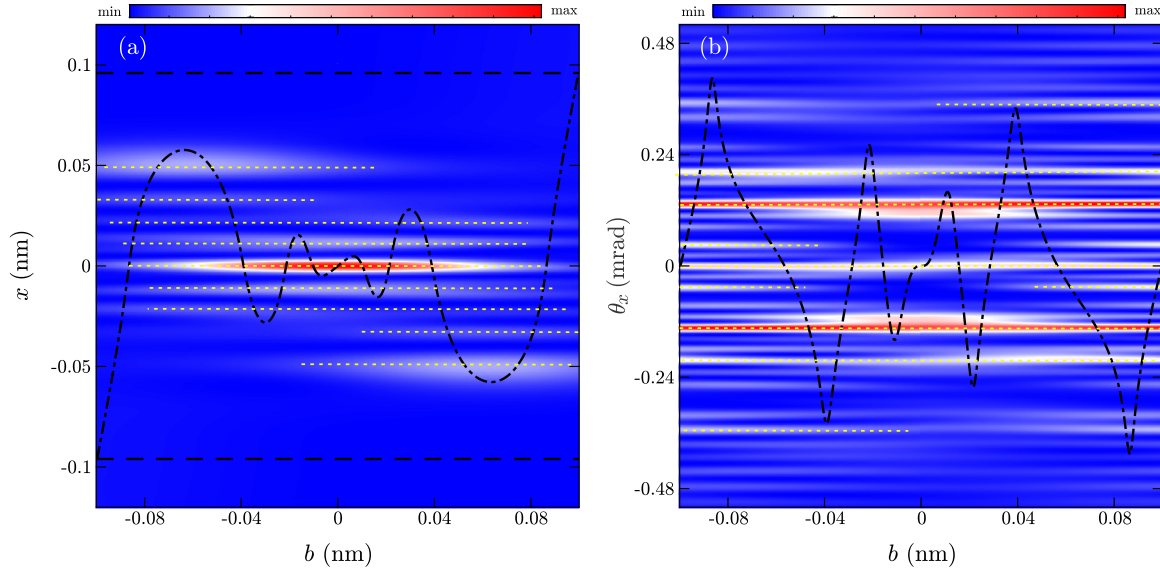


FIG. 7. The quantum deflection maps for $\Omega = 0.03\Theta_c$ at $\tau = 2$ in (a) spatial and (b) angular representations, respectively. Yellow (pale gray) dashed lines show coordination lines. Thick dot-dashed black lines show classical deflection functions. Dashed black lines show locations of atomic planes.

changes only slightly, while in the case of lines in Figs. 6(e) and 6(f) the change of the coordination angle is significant. Additionally, the number of coordination lines in the angular representation is greater than in the case of the spatial representation. While widths of self-interference peaks in the spatial representation are smaller than widths of peaks in the angular representation. This explains why evolution erases the information about the shape of individual wave packets more effectively in the case of spatial than in the case of angular distributions and provides an explanation why distributions of the electron beam shown in Fig. 4 are essentially classical.

To justify the presented interpretation we have investigated an evolution of the electron beam of the same energy but of much smaller angular divergence $\Omega = 0.03\Theta_c$. The resulting initial spatial standard deviation of the Gaussian wave packet is $\sigma_x = 43.18$ pm. The total width of the wave packet $6\sigma_x$ is now considerably larger than the width of the planar channel d_{220} . For this quantum ensemble, the dynamics of electron wave packets should depend only slightly on the impact parameter b .

For $\tau = 2$ quantum deflection maps in the spatial and angular representation are shown in Figs. 7(a) and 7(b), respectively. Dashed yellow lines show coordination lines only of prominent peaks. Note that all coordination lines are very long (much of them are even longer than $d_{220}/2$) while all coordination angles are $\phi \approx 0$. Because of the extremely weak dependence of the dynamics on the impact parameter, it is not possible to recognize classical deflection functions in quantum deflection maps.

The corresponding evolution of the electron beam in spatial and angular representation are shown in Figs. 8(a) and 8(b), respectively. According to the semiclassical interpretation, a cusp canonical diffraction pattern is associated with each pair of caustic lines [1,36,37]. This is clearly visible for $\tau < 0.75$ in Fig. 8(a) and for $\tau < 0.5$ in Fig. 8(b) since then there are no overlapping of neighboring canonical diffraction

patterns. Therefore obtained waveform can be understood as a superposition of four canonical cusp diffraction patterns, each associated with the respective classical caustic line pair. Figure 9 confirms that for $\phi = 0$, amplitudes of characteristic peaks formed by the self-interference are amplified by the ensemble. In this case, behavior of individual electrons and electron beam are both wavelike, as was expected from the start.

V. CONCLUSIONS

We have investigated the classical and the quantum dynamics of the 255-MeV electron beam transmitting through {220} planar channels of thin Si crystal.

In the classical approach, we have investigated how the period of the electron trajectories T depends on the impact parameter b and its relationship with the caustic pattern generated by the rainbow scattering. It has been shown that the repeating caustic motif consists of cusped lines. Their number, orientation, and position are determined by the number, type, and distribution of the function $T(b)$ critical points. Their interconnection is governed by the requirement that the overall pattern is structurally stable.

In the quantum approach, the electron beam was represented by the ensemble of the quantum wave packets which allowed us to investigate how beam divergence influences the dynamics of the electron beam. As a consequence electron beam also behaves wavelike. This is surprising since the dependence of the wave packet dynamics on the impact parameter was found to be weak but not negligible, and there are no a priori guarantees that small changes of the shape of wave packets would behave coherently. The situation is much more interesting in the case of an electron beam of moderate angular divergence. In that case, self-interference peaks of individual wave packets are mostly absent from the distributions of the ensemble. As a result, the shape of the

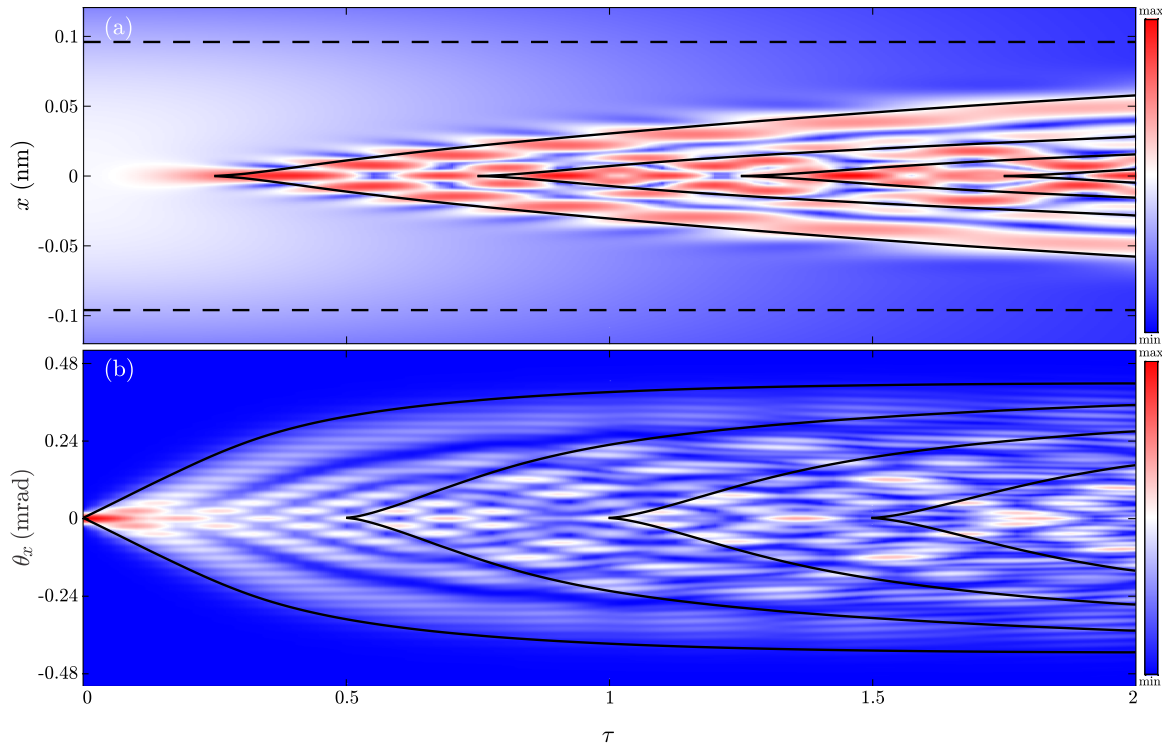


FIG. 8. The evolution of the probability density of the electron beam for $\Omega = 0.03\Theta_c$ transmitting through planar channels {220} of the Si crystal, in (a) spatial and (b) angular representations, respectively. Dashed black lines show locations of (220) planes. Thick black lines show classical caustic lines from Fig. 2.

resulting distributions of the electron beam reflects almost perfectly the shape of the classical caustic pattern. Thus the behavior of the electron beam is essentially classical. We have shown that the driving force behind this behavior is the tendency of the dynamics to induce the coherent change of the wave packet self-interference pattern for a small change

of its impact parameter. As a result wave packets self-interfere in a mutually coordinated way.

Note that the emergence of the classical structures is usually interpreted as a property of the high energy limit. It has been shown theoretically and confirmed experimentally that classical structures can emerge out of the underlying quantum

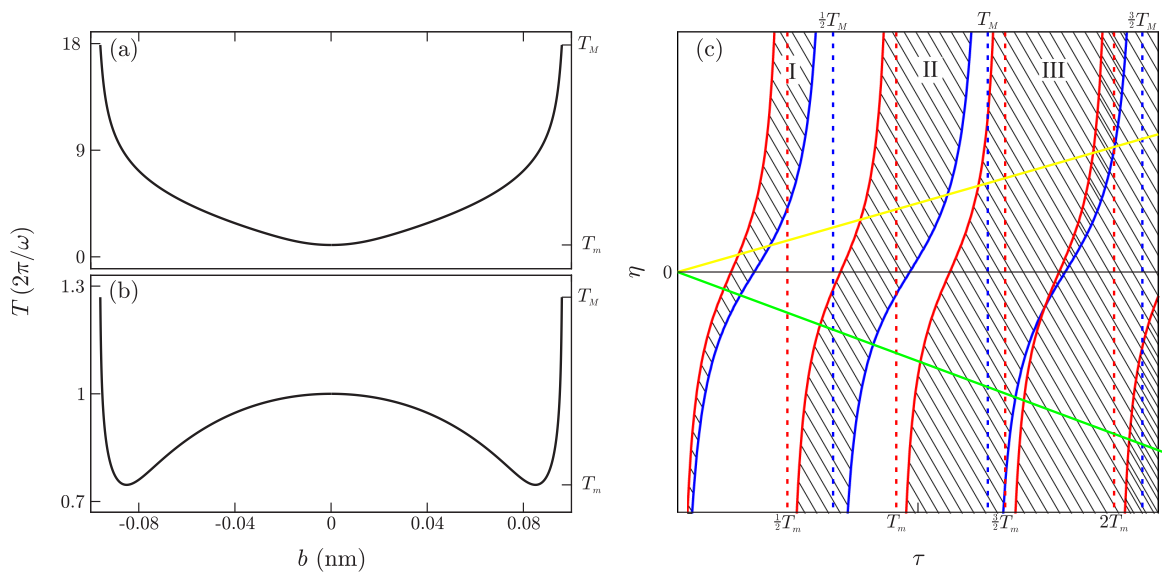


FIG. 9. The dependence of the period T of trajectory on the impact parameter b for 255-MeV (a) electrons and (b) positrons, transmitting through {220} planar channels of the Si crystal. (c) Schematic representation of the graphical method for the solution of the transcendental Eq. (A2).

dynamics without the need for the quantum behavior of wave packets to become classical. The quantum-classical transition happens in the ensemble for the fixed energy and represents an example of the deducible emergent property [55].

ACKNOWLEDGMENTS

The research was funded by the Ministry of Education, Science and Technological Development of the Republic of Serbia. The experimental part of this work was supported in part by JSPS KAKENHI Grant Number JP17K05483. This work was carried out partly using heterogeneous cluster Hybrilit at JINR (<http://hybrilit.jinr.ru/>).

APPENDIX A: ANHARMONICITY OF THE POTENTIAL AND THE CAUSTIC PATTERN

In the anharmonic potential, a period of the particle trajectory depends on the impact parameter. This dependency, defined by the integral (21), is called the anharmonicity function. Figures 9(a) and 9(b) show the anharmonicity functions $T_e(b)$ and $T_p(b)$ in the case of 255-MeV electron and positron beams, respectively. The function $T_e(b)$ has one minimum at the coordinate origin, while the function $T_p(b)$ have two symmetrical minima and one maximum at the coordinate origin. We shall show that a distribution of the anharmonicity function extrema directly determines the shape of the caustic pattern.

To simplify the analysis, we will model the trajectory family of the parallel beam by the relation

$$x_b(\tau) = b \cos \left[\frac{2\pi\tau}{T(b)} \right]. \quad (\text{A1})$$

The caustic condition $\partial_b x_b(\tau) = 0$ then reduces to the following transcendental equation:

$$2\pi \frac{\partial_b T(b)}{T^2(b)} b\tau = -\cot \left[\frac{2\pi\tau}{T(b)} \right]. \quad (\text{A2})$$

For any fixed value of the parameter b the left-hand side of Eq. (A2) represents a linear function $\eta = \alpha(b)\tau$ with a impact parameter dependent slope $\alpha(b) = 2\pi b \partial_b T(b)/T^2(b)$. The right-hand side of Eq. (A2) represents a negative cotangent function $\eta = -\cot[2\pi\tau/T(b)]$ of period $T(b)/2$. Note that if the considered range of the impact parameters is finite, as a consequence the range of values of the function $T(b)$ is also finite. Let us denote the shortest period in the range by T_m and the longest by T_M , and re-parameterize function families from Eq. (A2) by the variable T .

The right-hand side of Eq. (A2) defines now a family of negative cot functions continuously filling the space between function $-\cot(2\pi\tau/T_m)$ and $-\cot(2\pi\tau/T_M)$, and their periodic equivalents. These areas are in Fig. 9(c) shown schematically by the shaded regions between the red (gray) and the blue (dark gray) lines, respectively, labeled by an order of the periodic cycle. Because it is $T_M - T_m > 0$ sizes of shaded areas grow with the order of the cycle, and several neighboring regions can overlap with each other.

For clarity schematic representation in Fig. 9(c) is not drawn in any particular scale. In the case of positrons $T_M \approx 1.7T_m$. Region I is not overlapping with any other region, re-

gion II overlaps with region III, while region III overlaps with regions IV, V, VI, etc. In the case of electrons $T_M \approx 18T_m$. This implies that region I overlap with regions II, III, ..., XVIII, XVIII, etc.

In this new parametrization, a slope of lines defined by the left-hand side of Eq. (A2) is given by the expression $\alpha(T) = 2\pi b(T)/\partial_T b(T)T^2$. Note that map $T \rightarrow b$ is multivalued. For any point T , mentioned map is specified by a set of functions $b_s(T)$, $s \in 1, \dots, M(T)$, where $M(T)$ is a local multiplicity of the map. Therefore the left-hand side of Eq. (A2) define a set of straight lines $\eta = \alpha_s(T)\tau$, for $s \in 1, \dots, M(T)$.

In the case of electrons, $M(T) = 2$ for all T . Because of the inversion symmetry of the potential it is always $b_1(T) = -b_2(T)$, and $\alpha_1(T) = \alpha_2(T) \geq 0$. This double degenerate line is in Fig. 9(c) shown by the thick yellow (pale gray) line. In the case of positrons $M(T)$ can be 2 or 4 depending whether $T > 1$ or $T < 1$. When $M(T) = 2$ the situation is identical as in the case of electrons. When $M(T) = 4$, let four corresponding impact parameters be ordered in the following way $b_1 < b_2 < b_3 < b_4$. The symmetry of the potential requires that $b_1(T) = -b_4(T)$, $b_2(T) = -b_3(T)$, and $\alpha_1(T) = \alpha_4(T) > 0$ while $\alpha_2(T) = \alpha_3(T) < 0$. This additional double degenerate line of the negative slope is in Fig. 9(c) shown by the thick green (silver gray) line.

The $M(T)$ straight lines cross the curves $-\cot[2\pi\tau/T]$ in regions I, II, ... at points $\tau_s^I(T)$, $\tau_s^{II}(T)$, ..., for $s \in 1, \dots, M(T)$. In the τ - x space, this sequence generate points $(\tau_s^I, x_{b_s}(\tau_s^I))$; $(\tau_s^{II}, x_{b_s}(\tau_s^{II}))$, ... As a result, each of the regions I, II, ... gives $\max_T(M(T))$ branches of the caustic lines. In the case of electrons, each region gives two symmetrical branches of the caustic lines.

When the multiplicity of the map changes the number of the caustic lines also must change. To understand how this process happens, we need to investigate the behavior of the family (A1) in the vicinity of the extremum of the function $T(b)$. Let the local extremal value of the function $T(b)$ be T_0 located at point b_0 . In a neighbourhood of the point b_0 , function $T(b)$ can be represented by the following quadratic function $T(b) \approx T_0 + \gamma(b - b_0)^2$. Taylor expanding the multivariate function $x_b(\tau)$ up to the third-order around points $(b_0, T_0/4)$ gives

$$x_b(\tau) \approx \frac{2\pi}{T_0} \left(\frac{T_0}{4} - \tau \right) (b - b_0) + \frac{\pi\gamma}{2T_0} (b - b_0)^3. \quad (\text{A3})$$

It is easy to show that the behavior of the obtained family is equivalent to the behavior of the A_3 catastrophe defined by the relation [9,10]

$$A_3(\zeta; c_1, c_2) = \frac{\zeta^4}{4} + c_2 \frac{\zeta^2}{2} + c_1 \zeta, \quad (\text{A4})$$

where ζ represents the state variable while c_1 and c_2 are system parameters. The equilibrium set of the catastrophic family, defined by the equation $\partial_\zeta A_3(\zeta) = 0$, can be understood as an implicit definition of the following map

$$c_1 = -\zeta^3 - c_2 \zeta. \quad (\text{A5})$$

It is clear that substitutions $\zeta = -\sqrt[3]{\pi\gamma/2T_0}(b - b_0)$, $c_1 = x_b$ and $c_2 = \sqrt[3]{16\pi^2/T_0^2\gamma}(\tau - T_0/4)$ make families (A3) and (A5) identical. Caustic lines of the family (A3) are equivalent

to the bifurcation set $\partial_{\zeta}^2 A_3(\zeta) = 0$ of the A_3 catastrophe, which is in the parametric space given by the equation

$$\frac{c_1^2}{4^2} + \frac{c_2^3}{3^3} = 0, \quad (\text{A6})$$

and know as an equation of the cusp. Therefore, for $T \rightarrow T_0/4$, two branches of the caustic are born out of the cusp singular point or are annihilated at it, depending on whether a change of the multiplicity is $+2$ or -2 .

Now it is possible to explain the shape of the caustic pattern from Fig. 2(a). Since only minimum of the function $T_c(b)$ occurs for $b_0 = 0$ and $T_0 = T_m = 1$, symmetrical pairs of caustic lines emerge out of cusps points located at the axis of the planar channel which appear at times $\tau = 0.25, 0.75, 1.25, \dots$. Each pair is generated by intersection points of the green line from Fig. 9(c) and regions I, II, \dots . When intersection points reach the curve $\cot(2\pi/T_M)$ the caustic line terminates. In this particular case, the first caustic pair should exist at least for $\tau < 9$. A similar explanation applies to the evolution of other caustic lines.

In the case of positrons, the function $T_p(b)$ have three extrema. Therefore the repeating motif consists of three cusps. As in the previous case, four caustic branches emerge out of two symmetrically placed cusp points. The cusp corresponding to the maximum $T_0 = 1$ at $b_0 = 0$ must lie at the axis of the channel. In this case, two out of four branches must approach the τ axis, form a cusp for $\tau = 0.25$, and disappear afterward. The simplest elementary catastrophe composed of three cusps which satisfy the above stated constrains is the symmetrical family A_5 given by the relation

$$A_5(\zeta, c_1, c_2, c_3) = \frac{\zeta^6}{6} + c_4 \frac{\zeta^4}{4} + c_2 \frac{\zeta^2}{2} + c_1 \zeta, \quad (\text{A7})$$

also known as the butterfly. Its bifurcation set is completely identical with the caustic pattern obtained numerically (see Fig. 2 of the Ref. [12]).

In the case of caustics in the angular space, one could start from the following approximative function family

$$\theta_x(\tau; b) = -\frac{2\pi b}{\hbar k_z T(b)} \sin \left[\frac{2\pi \tau}{T(b)} \right]. \quad (\text{A8})$$

The analysis has shown that the same procedure applies to the analysis of angular caustic lines.

APPENDIX B: SEMICLASSICAL WAVE FUNCTIONS

For $\tau = 2$, spatial and angular deflection functions are in the vicinity of the impact parameter $b_0 = d_{220}/3$ approximated by the following polynomials:

$$\begin{aligned} \Theta_x(b) &= p_1(b - b_0) + p_0, \\ X(b) &= \frac{q_2}{2}(b - b_0)^2 + q_0, \end{aligned} \quad (\text{B1})$$

where $p_0 = -0.0858$ mrad, $p_1 = -23$ mrad/nm, $q_0 = -0.0636$ nm, and $q_2 = 1\,3964$ nm $^{-1}$. The corresponding reduced angular Hamilton's principal function is given by the following cubic polynomial:

$$\bar{S}_\theta(b) = \frac{r_3}{3}(b - b_0)^3 + r_1(b - b_0) + r_0, \quad (\text{B2})$$

whose coefficients are given by expressions $r_1 = p_1 q_0$ and $r_3 = p_1 q_2/2$, respectively. The constant r_0 is physically unimportant and it will be set to zero. To calculate integral (14) it is more convenient to make substitution $b - b_0 = u$. Using Eqs. (14) together with the initial distribution (11), it can be shown that the resulting integral is of the form

$$\psi_{b_0}(x) = \frac{\sqrt{k_z p_1}}{\sqrt[4]{8\pi^3 \sigma_x^2}} \int_{-\infty}^{\infty} \exp \left[-ik_z \left(\frac{r_3}{3} u^3 + \frac{i}{4\sigma_x^2 k_z} u^2 + (r_1 + p_1 x) u + p_0 x \right) \right] du. \quad (\text{B3})$$

Because of the rapid decrease of the Gaussian (11) validity of Eq. (B1) was extended to infinity. Using the following integral representation of the Airy function of the first kind

$$\text{Ai}(\beta - \alpha^2) = \frac{1}{2\pi} \exp \left[-i\alpha \left(\frac{2}{3} \alpha^2 - \beta \right) \right] \int_{-\infty}^{\infty} \exp \left[i \left(\frac{1}{3} \zeta^3 + \alpha \zeta^2 + \beta \zeta \right) \right] d\zeta, \quad (\text{B4})$$

which is convergent for purely imaginary parameter α [56] the semiclassical wave function becomes

$$\psi_{b_0}(x) = \sqrt[4]{\frac{\pi |p_1|^2}{2\Omega^2 |\gamma_1|^4}} e^{i\frac{\pi}{2}} \exp \left[\frac{1}{96\gamma_1^6} - \frac{p_1(x - q_0)}{8\gamma_1^3 \Omega} + ik_z p_0 x \right] \text{Ai} \left(\frac{1}{16\gamma_1^4} - \frac{p_1(x - q_0)}{2\gamma_1 \Omega} \right), \quad (\text{B5})$$

where $\gamma_1 = -\sqrt[3]{|r_3|/8\Omega^3 k_z^2}$ is dimensionless parameter.

APPENDIX C: THE CLASSICAL LIMIT OF THE SEMICLASSICAL WAVE FUNCTION

We shall now demonstrate, that the quantum wave function (B5) has the correct classical limit. In the semiclassical approach, the classical result is obtained as $k_z \rightarrow \infty$ limit. However, it is not correct to evaluate the limit in Eq. (B5) directly. The first thing to notice is that according to Eq. (7) parameter ω is k_z dependent. Therefore a larger value of the

variable k_z requires longer flight time t to keep the reduced time τ constant. This procedure makes parameters p_0, p_1, q_0 , and r_3 constant.

The second thing to notice is that the critical channeling angle Θ_c is also k_z dependent. If Ω is kept fixed then for some k_z it will be $\Omega > \Theta_c$, which makes Eq. (B5) invalid. To have equivalent physical reality for all values of the variable k_z it is necessary to assume that $\Omega = \kappa \Theta_c$, with κ kept constant.

The third thing to notice is that $\hbar k_z p_0$ is the quantum-mechanical mean value of the transverse linear momentum of the quantum state (B5), which is not affected by the change

of the shape of the wave function happening for different values of the k_z . The obtained value is precisely equal to the transverse linear momentum relativistic particle would have in the classical limit. Therefore it can be safely neglected from the further consideration of the classical limit of the wave function (B5).

Using the fact that in ultra-relativistic limit it is $E_k = c\hbar k_z$ Eq. (B5) can be rewritten in the following way

$$\psi_{b_0}(x) = \frac{\sqrt[4]{2\pi}|p_1|^{1/2}}{\lambda^{1/2}|r_3|^{1/3}} k_z^{5/12} \times \exp\left[\frac{k_z}{4\lambda^2|r_3|^{2/3}}(\zeta - \zeta_0)\right] \text{Ai}(k_z^{2/3}\zeta), \quad (\text{C1})$$

where

$$\lambda = \frac{1}{2\kappa} \sqrt{\frac{\hbar c}{V(d_{220}/2)}}, \quad \zeta = -\frac{|p_1|}{|r_3|^{1/3}} \left(x - q_0 - \frac{1}{16\lambda^4|p_1||r_3|}\right),$$

$$\zeta_0 = \frac{1}{48\lambda^4|r_3|^{4/3}}, \quad (\text{C2})$$

while physically unimportant constant phase factor has been neglected.

For $\zeta < 0$, i.e., for $x > q_0 + 1/16\lambda^4|p_1||r_3|$, the slowly decreasing amplitude of the Airy function oscillations are additionally damped by an exponential function. In the limit $k_z \rightarrow \infty$, the spacing between subsequent zeros of the airy function decreases by the factor $k_z^{2/3}$. As a consequence

$\psi_{b_0}(x)$ approaches the constant function 0 in the interval $q_0 + 1/16\lambda^4|p_1||r_3| < x < \infty$.

In the Ref. [56], it has been proven that for $\zeta > 0$

$$\text{Ai}(k_z^{2/3}\zeta) \leq \frac{\exp\left[-\frac{2}{3}k_z\zeta^{3/2}\right]}{2\sqrt{\pi}k_z^{1/6}\zeta^{1/4}}. \quad (\text{C3})$$

Therefore there is $\bar{\zeta}$, which is solution of the equation $-\frac{2}{3}\zeta^{3/2} + (\zeta - \zeta_0)/4\lambda^2|s_3|^{2/3} = 0$. For $\zeta > \bar{\zeta}$ the growth of an exponential factor in Eq. (C1) is overcompensated by a super-exponential decrease of the Airy function, while for $\zeta < \bar{\zeta}$ argument of the exponential factor is negative which completely overpowers very slow growth of the airy function for small arguments. In the limit $k_z \rightarrow \infty$, the wave function $\psi_{b_0}(x)$ tends again to the constant function 0 in observed intervals with a possible exception of the region in the vicinity of the point $\bar{\zeta}$. Since the norm of the state must be conserved the nonzero interval of the function ψ_{b_0} must shrink to zero while the corresponding value of the function ψ_{b_0} must increase. To estimate the rate of the divergence, it is sufficient to examine the behavior of the wave function at the point $\bar{\zeta}$. Using estimate (C3), we can conclude that in the limit $k_z \rightarrow \infty$ wave function $\psi_{b_0}(x)$ behaves as $k_z^{1/4}$. Therefore singularity indices β , σ_1 , and γ , introduced by Arnold and Berry to describe scaling of the amplitude, fringe spacing, and hypervolume in the parametric space are $\beta = 1/4$, $\sigma_1 = 2/3$, and $\gamma = 2/3$, respectively [57,58].

-
- [1] M. V. Berry and K. V. Mount, *Rep. Prog. Phys.* **35**, 315 (1972).
[2] M. V. Berry, *Chaos et Physique Quantique/Chaos and Quantum Physics*, edited by M. J. Giannoni, A. Voros, and J. Zinn-Justin, Les Houches Lecture Series Session LII (North-Holland, Amsterdam, 1989), pp. 251–304.
[3] M. V. Berry, *Asymptotics, Singularities and the Reduction of Theories*, edited by D. Prawitz, B. Skyrms, and D. Westerstahl, Proc. 9th Int. Cong. Logic, Method. and Phil. of Sci. IX, pp. 597–607 (1994).
[4] M. V. Berry (private communication).
[5] J. von Neumann, *Mathematical Foundations of Quantum Mechanics* (Princeton University Press, Princeton, 1955).
[6] W. H. Zurek, *Rev. Mod. Phys.* **75**, 715 (2003).
[7] M. Čosić, S. Petrović, and S. Bellucci, *Sci. Rep.* **10**, 1 (2020).
[8] R. Thom, *Structural Stability and Morphogenesis* (Logos, Mocsow, 2002) [russian edition].
[9] V. I. Arnold, *Catastrophe Theory* (Springer-Verlag, Berlin, Heidelberg, 1986).
[10] T. Poston and I. Stewart, *Catastrophe: Theory and Its Applications* (Pitman, London, 1978).
[11] D. S. Gemmell, *Rev. Mod. Phys.* **46**, 129 (1974).
[12] M. Čosić, N. Nešković, and S. Petrović, *Nucl. Instrum. Methods Phys. Res. Sect. B* **444**, 10 (2019).
[13] S. Petrović, M. Čosić, and N. Nešković, *Phys. Rev. A* **88**, 012902 (2013).
[14] J. A. Adams, *Phys. Rep.* **356**, 229 (2002).
[15] J. N. L. Connor and D. Farrelly, *J. Chem. Phys.* **75**, 2831 (1981).
[16] F. Michel, G. Reidemeister, and S. Ohkubo, *Phys. Rev. Lett.* **89**, 152701 (2002).
[17] H. Winter and A. Schüller, *Prog. Surf. Sci.* **86**, 169 (2011).
[18] D. Borka, S. Petrović, and N. Nešković, *Channeling of Protons through Carbon Nanotubes* (Nova Science, New York, 2011).
[19] N. Nešković, S. Petrović, and M. Čosić, *Rainbows in Channeling of Charged Particles in Crystals and Nanotubes* (Springer, Berlin, 2017).
[20] M. Čosić, S. Petrović, and N. Nešković, *Nucl. Instrum. Methods Phys. Res. B* **422**, 54 (2018).
[21] H. F. Krause, S. Datz, P. F. Dittner, J. Gomez del Campo, P. D. Miller, C. D. Moak, N. Nešković, and P. L. Pepmiller, *Phys. Rev. B* **33**, 6036 (1986).
[22] M. Motapothula, S. Petrović, N. Nešković, Z. Y. Dang, M. B. H. Breese, M. A. Rana, and A. Osman, *Nucl. Instrum. Meth. Phys. Res. B* **283**, 29 (2012).
[23] S. Petrović, N. Nešković, M. Čosić, M. Motapothula, and M. B. H. Breese, *Nucl. Instrum. Meth. Phys. Res. B* **360**, 23 (2015).
[24] M. Motapothula, S. Petrović, N. Nešković, Z. Y. Dang, M. B. H. Breese, M. A. Rana, and A. Osman, *Phys. Rev. B* **86**, 205426 (2012).
[25] M. Motapothula, S. Petrović, N. Nešković, and M. B. H. Breese, *Phys. Rev. B* **94**, 075415 (2016).
[26] S. P. Fomin and N. F. Shul'ga, *Phys. Lett. A* **73**, 131 (1979).
[27] N. F. Shul'ga and S. N. Shul'ga, *Phys. Lett. B* **769**, 141 (2017).

- [28] S. N. Shul'ga, N. F. Shul'ga, S. Barsuk, I. Chaikovska, and R. Chehab, *Nucl. Instrum. Methods Phys. Res. Sect. B* **402**, 16 (2017).
- [29] M. Ćosić, S. Petrović, and N. Nešković, *Nucl. Instrum. Methods Phys. Res. Sect. B* **373**, 52 (2016).
- [30] M. Ćosić, S. Petrović, and N. Nešković, *Nucl. Instrum. Methods Phys. Res. Sect. B* **399**, 1 (2017).
- [31] Y. Takabayashi, Y. L. Pivovarov, and T. A. Tikhfatullin, *Phys. Lett. B* **785**, 347 (2018).
- [32] G. Molière, *Z. Naturforsch.* **2a**, 133 (1947).
- [33] T.-Y. Wu and T. Ohmura, *Quantum Theory of Scattering* (Prentice Hall, New Jersey, 1962).
- [34] B. R. Appleton, C. Erginsoy, and W. M. Gibson, *Phys. Rev.* **161**, 330 (1967).
- [35] M. Abramowitz and I. Stegun, in *Handbook of Mathematical Functions* (National Bureau of Standards, Washington, 1972), p. 302.
- [36] M. Ćosić, S. Petrović, and S. Bellucci, *Chaos* **30**, 103107 (2020).
- [37] M. V. Berry and C. Upstill, in *Catastrophe Optics: Morphologies of Caustics and Their Diffraction Patterns*, edited by E. Wolf, Progress in Optics (North-Holland, Amsterdam, 1980), Vol. XVIII, pp. 257–346.
- [38] W. H. Miller, *J. Chem. Phys.* **53**, 1949 (1970).
- [39] K. G. Kay, *Annu. Rev. Phys. Chem.* **56**, 255 (2005).
- [40] R. M. Sternheimer, *Phys. Rev.* **145**, 247 (1966).
- [41] V. M. Biryukov, Y. A. Chesnokov, and V. I. Kotov, *Crystal Channeling and Its Application at High-Energy Accelerators* (Springer, Berlin, Heidelberg, 1997).
- [42] J. D. Jackson, *Classical Electrodynamics* (Wiley, Hoboken, New Jersey, 1999).
- [43] V. I. Arnold, *The Theory of Singularities and Its Applications* (Accademia Nazionale dei Lincei, Pisa, 1991).
- [44] V. I. Arnold, *Singularities of Caustics and Wave Fronts* (Springer-Verlag, Berlin, Heidelberg, 1991).
- [45] W. Press, S. Teukolsky, W. Vetterling, and B. Flannery, *Numerical Recipes in FORTRAN* (Cambridge University Press, Cambridge, 1993).
- [46] L. Miletić, S. Petrović, and N. Nešković, in *Contributed Papers of the 18th Summer School and International Symposium on the Physics of Ionized Gases*, edited by B. Vujičić and S. Djurović (Novi Sad: Faculty of Sciences, Institute of Physics, Kotor, Yugoslavia, 1996), pp. 161–164.
- [47] M. V. Berry and D. H. J. O'Dell, *J. Phys. A: Math. Gen.* **32**, 3571 (1999).
- [48] J. W. Bruce and P. J. Giblin, *Curves and Singularities* (Cambridge University Press, Cambridge, 1984).
- [49] R. Kosloff, *J. Chem. Phys.* **92**, 2087 (1988).
- [50] M. Ćosić, S. Petrović, and N. Nešković, *Nucl. Instrum. Methods Phys. Res. Sect. B* **330**, 33 (2014).
- [51] J. E. Bayfield, in *Niels Bohr Collected Works*, edited by L. Rosenfeld and J. R. Nielsen, Vol. 3 the Correspondence Principle (1918-1923) (North-Holland, Amsterdam, 1976).
- [52] J. F. Nye, in *Natural Focusing and Fine Structure of Light: Caustics and Wave Dislocations* (IOP Publishing, Bristol, 1999), p. 132.
- [53] H. M. Nussenzveig, *Diffraction Effects in Semiclassical Scattering* (Cambridge University Press, Cambridge, 1992), pp. 105–107.
- [54] W. H. Zurek, *Nature* **412**, 712 (2001).
- [55] N. A. Baas and C. Emmeche, *Intellectica* **2**, 67 (1997).
- [56] O. Valle'e and M. Soares, in *Airy Functions and Applications to Physics* (World Scientific, New Jersey, 2004), p. 10.
- [57] V. I. Arnol'd, *Russian Math. Surveys* **30**, 1 (1975).
- [58] M. V. Berry, *J. Phys. A: Math. Gen.* **10**, 2061 (1977).